The Electrochemical Society
Advancing solid state & electrochemical science & technology

Entropy Profiling for the Diagnosis of NCA/Gr-SiOx Li-Ion Battery Health

View the article online for updates and enhancements.

Entropy Profiling for the Diagnosis of NCA/Gr-SiOx Li-Ion Battery Health

Malgorzata E. Wojtala,[1] Alana A. Zülke,[2,3] Robert Burrell,[2,3] Mangayarkarasi Nagarathinam,[2,3] Guanchen Li,[4] Harry E. Hoster,[2,3,5] David A. Howey,[1,3] and Michael P. Mercer[2,3,z]

[1]*University of Oxford, Department of Engineering Science, Parks Road, Oxford, OX1 3PJ, United Kingdom*
[2]*The Faraday Institution, Harwell Campus, Didcot OX11 0RA, United Kingdom*
[3]*Lancaster University, Department of Chemistry, Lancaster LA1 4YB, United Kingdom*
[4]*University of Glasgow, James Watt School of Engineering, Glasgow G12 8QQ, United Kingdom*
[5]*The Hydrogen and Fuel Cell Center ZBT GmbH, Duisburg, 47057 Duisburg, Germany*

Graphite-silicon (Gr-Si) blends have become common in commercial Li-ion battery negative electrodes, offering increased capacity over pure graphite. Lithiation/delithiation of the silicon particles results in volume changes, which may be associated with increased hysteresis of the open circuit potential (OCP). The OCP is a function of both concentration and temperature. Entropy change measurement—which probes the response of the OCP to temperature—offers a unique battery diagnostics tool. While entropy change measurements have previously been applied to study degradation, the implications of Si additives on the entropy profiles of commercial cells have not been explored. Here, we use entropy profiling to track ageing markers in the same way as differential voltage analysis. In addition to lithiation/delithiation hysteresis in the OCP of Gr-Si blends, cells with Gr-Si anodes also exhibit differences in entropy profile depending on cycling direction, reflecting degradation-related morphological changes. For cycled cells, entropy change decreased during discharge, likely corresponding to graphite particles breaking and cracking. However, entropy change during charge increased with cycling, likely due to the volume change of silicon. Over a broad voltage range, these combined effects led to the observed rise in entropy hysteresis with age. Conversely, for calendar aged cells entropy hysteresis remained stable.

Li-ion batteries (LiBs) have successfully made the leap from small portable devices to large-scale applications, where multi-cell arrangements must be effectively monitored and controlled by a battery management system (BMS) to guarantee durable and safe operation.[1,2] The BMS requires reliable inference of state-of-charge and state-of-health (SoC and SoH), especially as LiBs age. Currently, inaccurate SoC and SoH algorithms are compensated for by over-designing battery packs and keeping conservative operational limits, which reduces energy efficiency and increases costs and carbon footprint. Research on how to model degradation using only the available measurements provided by the BMS (voltage, current and temperature) is therefore fundamental to accelerate battery innovation, and there is a rising demand for ageing data and models.[3–5]

Especially important is the need for electrochemistry-aware models with the potential to inform better decisions around use strategies, second-life applications, and ultimately, optimized battery designs and systems. This requires an understanding of the (electro) chemical signatures of degradation. Although the microscopic origins of degradation are numerous and complex,[6–8] on a macroscopic level performance loss manifests as capacity reduction and buildup of resistance.[9,10] While the former is related to loss of storage capability and associated with lost lithium inventory (LLI) and/or change of active material microstructure (LAM), the latter results from increased impedance at all interfaces within the individual cells and across pack connections.

At lab-scale, various non-invasive techniques can be used (and combined[11]) for classifying the above-mentioned degradation modes. One of the methods monitors electrode slippage, which refers to the shift of capacity of anode versus cathode relative to their alignment in a pristine cell.[12,13] It is also common to differentiate

voltage and capacity curves obtained near equilibrium conditions to quantify peak shifts and classify degradation.[14,15] These methods are known as differential voltage analysis (DVA), defined as dV/dQ, and incremental capacity analysis (ICA), calculated as dQ/dV. These are well-established methods for degradation mechanism identification.[14,15] However, so far the application of these methods to degradation has been based only on LAM/LLI, without further microstructural interpretation.[16–18] Additionally, all these methods are performed at constant temperature, however, temperature dependence also contains information relevant to degradation. Given that the OCP is a function of both concentration and temperature, neglecting one of these dependencies in ageing diagnostics is limiting. In this regard, thermal and voltage analysis, obtained e.g. via differential thermal voltammetry (DTV), can provide an insight into ageing mechanisms.[19] However, the resultant curves depend on galvanostatic cycle rate and hence it is non-trivial to interpret them from a microstructural perspective.

The measurement of entropy changes, known as entropy profiling, is another method that has been proposed for understanding degradation.[20–23] Maher and Yazami[21] explored cycle ageing of a LCO/Gr cell, finding changes in the entropy profiles associated with loss of battery capacity, but there was no clear trend observed in the entropy profile changes. Using Raman spectroscopy, changes in the entropy profiles were attributed to crystallographic changes in the cathode material with ageing. Sullivan et al.[20] focused on LCO half-cell analysis. A clear trend was observed: with prolonged cycling, the characteristic LCO entropy profile features (maximum and minimum) became less pronounced. They attributed changes in the entropy curves to changes in lithium ordering resulting from ageing. Entropy profiling of aged cells was also performed by Zhang et al.[22] and Osswald et al..[23] Zhang et al. examined LCO/Li half-cells while Osswald et al. looked at cylindrical 18 650 NCA/Gr and NMC/Gr cells. However, neither study offered interpretation of the changes in entropy features with ageing.

[z]E-mail: m.mercer1@lancaster.ac.uk

Table I. Samsung 35E specifications.

Cell model	INR18650-35E
Cathode chemistry	LiNi$_{0.8}$Co$_{0.15}$Al$_{0.05}$O$_2$ (NCA)
Anode chemistry	Gr-SiO$_x$ (∼10 wt % SiO$_x$ and ∼90 wt % Gr)
Nominal capacity	3.4 Ah
Cut-off voltage	4.2 V/ 2.5 V

Just as voltage versus SoC data has been shown to depend on cycling direction,[15,24–27] the partial molar entropy (or entropy change) related to the variation of the OCP with temperature also shows a directional path dependency.[24,25] This type of hysteresis is found even in half-cell studies of lithium (de)insertion from graphite anodes.[25,28] The addition of silicon or silicon suboxide (SiO$_x$) to graphite to form a blended anode material leads to greater OCP hysteresis than in graphite-only anodes.[15,26,27] A greater mass fraction of SiO$_x$ leads to an even greater observed hysteresis.[29] The physical relationship between OCP hysteresis and entropy has been shown by Assat et al.[24] for a single cell chemistry at the beginning of cell life, but the entropy hysteresis might also depend on the long term history of the cell and related microscopic changes due to ageing.

We postulate that entropy profiling is a unique non-invasive battery diagnostic tool that provides the same information about ageing as DVA, but in addition elucidates morphological changes experienced by a battery throughout its life. We investigate this by comparing entropy profiles from pristine, accelerated calendar-aged, and cycle-aged cells. We find that there is hysteresis in the entropy change at the start of cell life, and this hysteresis does not change significantly for calendar aged cells, but increases with cycle ageing. We hypothesize that these differences originate from microscopic material changes that reflect the unique ageing history.[20,30] Finally, as far as we know, no NCA-Gr|SiO$_x$ entropy ageing curves are available in the literature, so this work provides such data. The case of a silicon-doped anode is particularly interesting from the thermodynamic point of view, given its volume variation during (de)intercalation.

Background

Entropy in batteries.—Entropy changes in batteries are directly linked to the reversible heat generated or consumed during charge or discharge reactions,[24,31] and the entropy of reaction may be related to the open circuit voltage according to

$$\left.\frac{\partial(\Delta S)}{\partial x}\right|_{p,T} = nF\left.\frac{\partial E_{OCP}}{\partial T}\right|_{p,x}, \qquad [1]$$

where ΔS is the entropy of the cell reaction, x is the extent of the reaction (in this case, degree of lithiation in the insertion electrodes), F is the Faraday constant, $n = 1$ is the number of electrons transferred in the reaction, E_{OCP} is the open circuit potential of the cell, with both electrodes combined, T is the absolute temperature, and p denotes pressure, which is usually assumed constant for battery systems.

Mechanical effects are often neglected in the majority of electrode materials, but in the specific case of silicon they are likely important due to its high volumetric expansion[32]—this aspect will be discussed later together with its implications. Abrupt energy changes accompanying first order phase transitions result in rapid changes in OCP gradient at these points. Since phase change is always associated with changes in thermodynamic properties, we might reasonably expect to see correspondence between features present in DVA and also features in entropy of reaction changes with respect to stoichiometry.

In a stable, fully reversible charge-discharge cycle, the result of the integration of entropy change around a closed cycle would be zero. However, according to the second law of thermodynamics, for a real battery system, a charge-discharge cycle cannot be thermodynamically reversible above 0 K. Given that heat production rate equals electrical work performed by the cell, Assat et al.[24] identified that entropy production relates to the observed voltage hysteresis. Therefore, in addition to the hysteresis measured in OCP curves, one also measures a hysteresis associated with entropy measurements.[24,25,28] This source of hysteresis is always present in a metastable system.[24]

The variation of partial molar entropy, ($\partial\Delta S/\partial x$), as defined in Eq. 1, is predominantly determined by lithium/vacancy configurations and is thus sensitive to the host electrode microstructures.[31,33–35] The measured OCP difference with cycling direction is sensitive to the electrode microstructure in several systems[25,26,36] and is thus reasonable to postulate that the entropy change hysteresis shows similar sensitivity. This means that measuring entropy changes and their variation with cycle direction may allow the tracking of structural defects, volume and ordering changes dependent on ageing conditions.

Impact of adding silicon to graphite anode.—Numerous studies agree that monitoring the evolution of peaks and valleys present in entropy vs. capacity graphs over a cell's lifetime may be used for degradation diagnosis.[20–22] However, the introduction of silicon to the anode material introduces additional challenges for characterization because of the much greater OCP hysteresis found during lithiation/delithiation of silicon than in pure graphite anode materials.[15,26,27]

While for graphite the total volume expansion from a fully delithiated to fully lithiated state is small (∼10%), and confined to one crystallographic axis,[37,38] silicon is reported to experience ∼300%–400% volume expansion[29,32,39] during lithiation, followed by a contraction in delithiation. Sullivan et al. found that particle cracking, and hence a decrease in the mean active particle size, leads to visible changes in entropy curves.[20] This finding suggests that there could be an association between particle size and entropy profile features. In the case of silicon, therefore, the large changes in volume during lithiation/delithiation could be associated with changes to the measured hysteresis during cycling.

Vorauer et al.[40] used post-mortem small-angle neutron scattering which produces intensity versus scattering vector (Q) plots to visualise the (de)lithiation structural changes of an amorphous silicon (a-Si) /crystalline iron-silicide graphite composite anode. They observed no nanoscale swelling of a-Si with cycling after lithiation. However, anode delithiation was followed by a high-Q intensity decrease due to a-Si shrinkage, which did not reverse back to its initial value. Instead, the intensity in the aged sample remained slightly higher than the pristine sample, which means that the a-Si phase remained more expanded.[40]

Also, the rate of SEI growth is higher in silicon doped anodes[41] than in anodes without silicon. The change in silicon particle size with cycling exerts a mechanical strain on the SEI layers, causing cracking and exposure of fresh active material to the electrolyte.[42] Furthermore, neutron reflectometry studies performed by Veith et al.[41] indicate that the SEI on silicon restructures during lithiation/delithiation. During delithiation, Si particles contract and the SEI becomes dispersed in the matrix pores, leading to a lower electrical conductivity and limits access of Li to the active particles.

As a consequence of these irreversible volume changes during lithiation/delithiation, the hysteresis in the OCP and entropy change are both expected to vary with cycling ageing. During calendar storage, where no repetitive volumetric changes occur, the hysteresis is expected to remain stable throughout life.
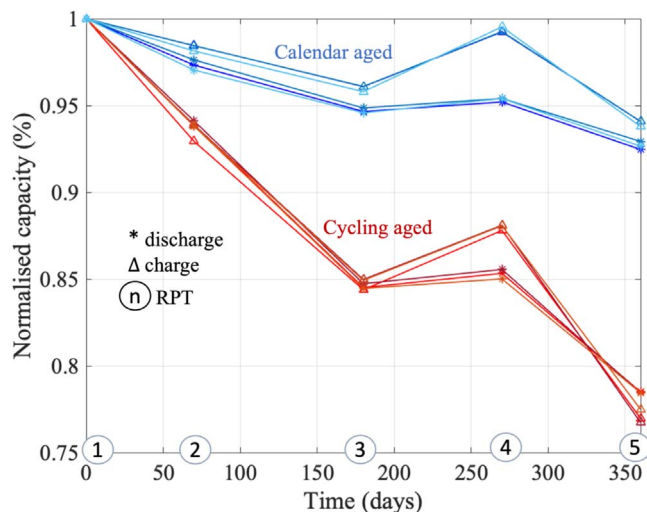
Figure 1. Observed capacity loss through RPTs for calendar and cycle aged cells for charge and discharge. The encircled numbers 1–5 in the Fig. refer to the RPT number. All cells experienced a 3 months rest period at 23 °C and 50% SoC between RPT3 and RPT4 due to COVID-19 lab closure.

Experimental

Experimental setup.— Full-cells.—Commercially available Li-ion cells (Samsung 35E3) with high silicon content (∼10 wt % Si and ∼90 wt % Gr) were used, with specifications given in Table I. All cells tested were from the same manufacturing batch, purchased in 2018. Screening tests at beginning of life for the entire group of cells (178 units) revealed a mean discharge capacity of 3.40 ±0.01 Ah, measured at C/3 and 23 °C. The cells were divided into two groups of three cells each. The first group was stored at elevated temperature to act as an accelerated calendar ageing example, while the second group underwent cycle ageing tests.

A high-precision battery tester (HPC 10, Battery Dynamics) was used for battery cycling, with NTC (5 k Ω) thermistors mechanically attached to the cell surfaces using O-rings for temperature recording. For temperature control, all cells were submerged in a thermostatic bath (Corio CD 900F, Julabo) filled with polydimethylsiloxane (PDMS, H5 bath fluid, Julabo).[43]

Half-cells.—To investigate individual electrode entropy contributions, several half-cells were manufactured. A pristine full-cell was fully discharged to 2.5 V at C/25 constant current and disassembled in an Argon-filled glove-box (MBraun). The harvested electrode material from the anode and cathode foils was punched into 14 mm diameter discs and re-assembled into coin cells with metallic lithium discs (Xiamen Tob New Energy Technology) as the other electrode, using pre-dried LP30 (Sigma Aldrich) as electrolyte and glass microfiber filters (grade GF/F, Whatman) as separators.

Electrochemical characterization for the anode and cathode half-cells was performed using a BaSyTec CTS cycler. Experimental measurements were performed using aluminum heat exchangers, in direct thermal contact with the coin cells, which were connected to a Julabo F12 refrigerated—heating circulator, allowing direct control over the cell temperatures. This setup enabled more rapid thermal equilibration of the cells than would be possible using a climate chamber. Cell temperatures were monitored with type-T thermocouples. A Keysight 34 972A data acquisition system with multiplexer unit was used for high resolution (22 bit) voltage and temperature measurements, assisting post processing of entropy profile data, as described in previous publications.[23,25,35,44,45]

All half-cells were allowed a 24-hour rest period following cell manufacture, to ensure proper wetting of the electrodes. For the anode half-cells, three consecutive cycles at cycle rate 27 mA g^{-1} (normalised to the mass of active material of each electrode) were

undertaken for loading and conditioning, at 25 °C. Subsequent to the galvanostatic cycles, cells were subjected to constant current constant voltage (CCCV) protocols at 25 °C. Anode half-cells were discharged at 27 mA g^{-1} until reaching a cell voltage of 0.005 V versus Li, and were subsequently held at 0.005 V for 2 h. After manufacture and rest, cathode half-cells were cycled three times at 13.5 mA g^{-1}, followed by CCCV at 13.5 mA g^{-1}, terminating at 4.3 V vs. Li for 2 h. Both sets of half-cells then underwent an accelerated entropy measurement procedure (further details in Section Accelerated entropy measurement technique).

Ageing tests.—The first group of full-cells experienced one year of calendar ageing at 75% SoC and 45 °C and the second group underwent continuous cycling (up to ∼720 cycles) with 2 A constant current charging until 4.2 V and 2 A constant current discharge until 2.5 V at 45 °C.

Both groups of full-cells (calendar and cycle aged) underwent periodic characterization tests, specifically reference performance tests (RPTs) to measure capacity and psuedo-OCV data. The RPT consisted of a full charge and discharge at C/20 at 23 °C. This was followed by a non-isothermal galvanostatic intermittent titration technique (GITT) for accelerated entropy measurement. The non-isothermal GITT procedure is described in Sect. 3.3.

Figure 1 shows the capacity fade in both the calendar and cycle aged groups, measured by the RPTs. Due to a lab closure caused by COVID-19, all cells experienced an unplanned rest period of 3 months at 50% SoC and 23 °C. The resulting capacity recovery between RPT3 and RPT4 is shown in Fig. 1; the implications of this effect for the interpretation of the results is discussed later in the text.

Accelerated entropy measurement technique.—To investigate entropy changes during battery ageing, an accelerated measurement method proposed by Osswald et al.[23] was used. Compared to the conventional potentiometric method, which requires up to 30 h relaxation time per SoC point,[22] the accelerated method shortens this to 2.5 h per SoC evaluation.

The accelerated entropy measurement method uses curve fitting to correct for small changes in the open circuit voltage as it equilibrates, thus decreasing the required rest times. (As an aside, it is not possible to obtain the true equilibrium potential over a practical timescale anyway;[25,26,37,46–48] this means we can, at best, probe metastable behavior). To avoid measurement artefacts, two steps were taken. Firstly, the initial rest period of 20 min following a temperature change was sufficiently long to ensure uniform cell internal temperature. Secondly, the background voltage change was subtracted from the temperature induced changes.[23] For full-cells, we used 63 titration steps (0.3 A current between steps) during both charge and discharge excursions including subsequent 80 min of relaxation, until the potential reached the respective cutoff voltage. During the GITT relaxation steps, temperature jumps of 28 , 25 and 22 °C were included, shown in Fig. 2. To promote rapid and uniform heat exchange with the environment, the cells were submerged in a silicone oil thermal bath.

For half-cells, the same GITT relaxation steps and temperature profile were used as for the full-cells. During titration steps, the current of the cathode half-cells was set to 13.5 mA g^{-1} (discharge) and the anode half-cells was set to 27 mA g^{-1} (charge), to account for the factor of ≈2 difference between anode and cathode half-cell capacity.

SEM/EDX and coating thickness analysis.—A pristine, calendar aged, and cycle aged full-cell were fully discharged to 2.5 V at C/10 constant current and disassembled in an Argon-filled glove box (Inert PureLab HE). Scanning electron microscopy (SEM) measurements were performed with a JEOL JSM 6500F, which was operated at low voltage (5 kV) to highlight the surface details. Subsequently, a JEOL JSM 6480LV (15 kV) SEM was used to obtain energy-dispersive X-ray spectroscopy (EDX) maps. The SiO$_x$ particle size range was determined by measuring all the coloured
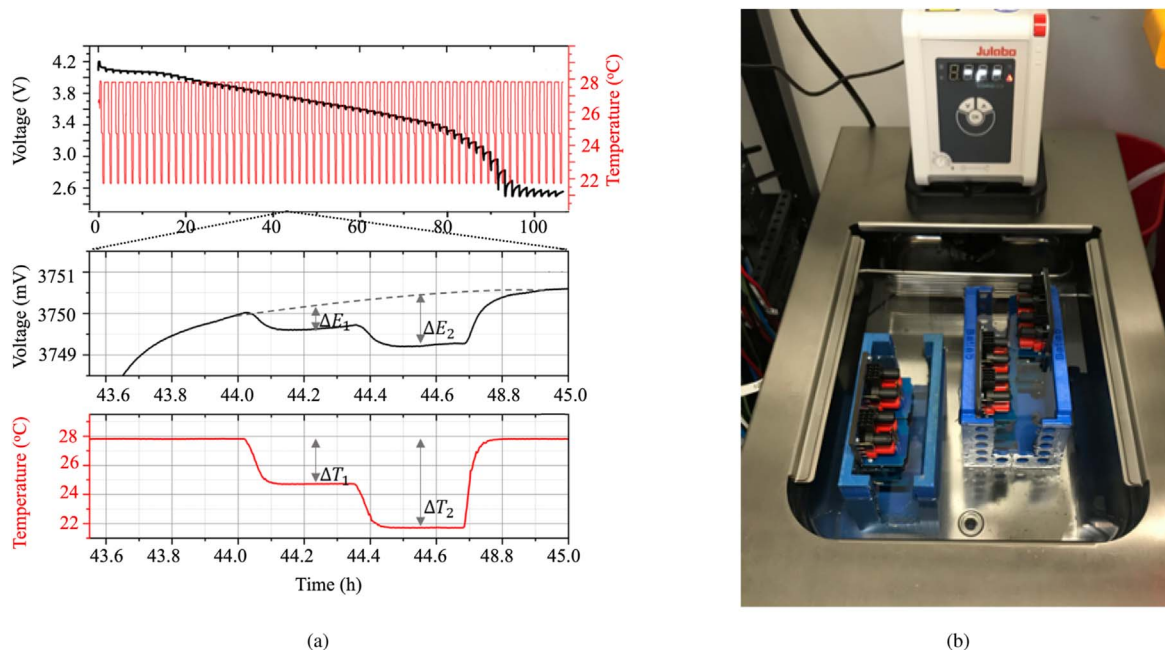
Figure 2. Accelerated entropy profiling experiment during a complete discharge (a). Zoomed regions indicates the deviation of the cell terminal voltage from the expected value (dashed line), caused by the temperature-step. Experimental setup showing the location of the cells in the direct-cooling apparatus is shown in (b).

particles representing the element Si in a 2D EDX image (Supplementary MaterialFig. S2).

A micrometer with 0.001 mm resolution and ±0.002 mm accuracy was used to measure coating thicknesses of the electrode material harvested from the full-cells. The coating thickness was determined by taking an average of three samples from different locations on the electrode.

Results and Discussion

Half-cell entropy contributions.—Measurements of half-cell reaction entropy may be summed to obtain the full-cell entropy change (as defined in Eq. 1), enabling features to be attributed to an individual electrode, as shown in Fig. 3. The full-cell entropy change comprises cathode S_c and anode S_a contributions

$$\left.\frac{\partial(\Delta S)}{\partial x}\right|_{p,T} = \left.\frac{\partial(S_c)}{\partial x}\right|_{p,T} - \left.\frac{\partial(S_a)}{\partial x}\right|_{p,T}, \qquad [2]$$

which are defined similarly to Eq. 1.

During lithium intercalation, the open circuit potential of the Li-graphite system measured with respect to Li/Li$^+$ declines through a succession of sloping and flat regions that result from the staging process: single-phase transitions are the slopes and two-phase transitions correspond to flat regions.[15,25,35,49] Although the anode material contains SiO$_x$, during anode delithiation the anode related features are very similar to reported responses for lithium insertion into pure graphite.[25,35] First, the Li+ inserts into the spaces between each graphite layer in the anode host. Increasing Li+ concentration drives the Li-graphite system into dilute stage IV structures, followed by dilute stage III structures. However, these stages are weakly ordered and so the entropy change follows an ideal solid solution response in these regions.[35] Hence, at low lithium occupation in the anode (scaled capacity less than 1.5 Ah in Fig. 3), the $\frac{\partial S_a}{\partial x}$ rises as lithium is inserted. Over the same capacity range, there is a small feature in $\frac{\partial S_c}{\partial x}$, but the cathode entropy profile otherwise remains relatively featureless.

Additional incorporation of Li+ into graphite results in a two-phase region between about 1.5 Ah and 2.25 Ah capacity, where LiC$_{12}$ and LiC$_{18}$ coexist. There is therefore a voltage plateau, and
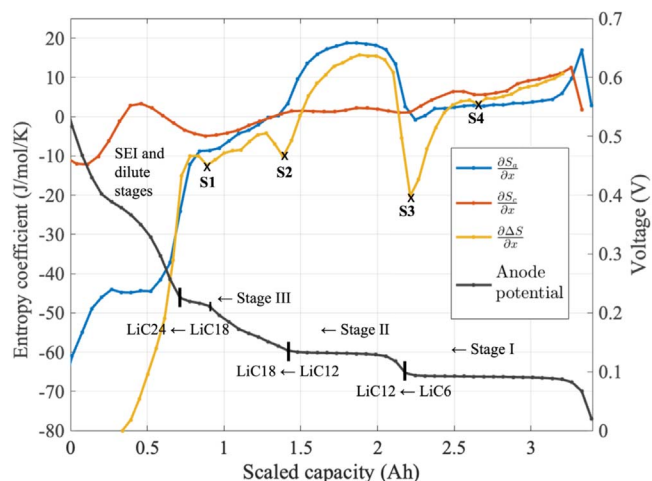
Figure 3. Entropy profiles for anode (Gr/Si), cathode (NCA), and a full-cell cell at the beginning of life. The entropy coefficient on the left *y*-axis refers to the $\frac{\partial S_a}{\partial x}, \frac{\partial S_c}{\partial x}, \frac{\partial \Delta S}{\partial x}$ respectively. The black line marking the anode OCP uses the right-*y* axis. Characteristic full-cell entropy features S1-S3 correspond to anode OCP staging.

similarly the $\frac{\partial S_a}{\partial x}$ shows a transition at about 1.5 Ah capacity and then the entropy response remains nearly constant over the two-phase region. At about 2.25 Ah, a transition to LiC$_{12}$-LiC$_6$ coexistence occurs and $\frac{\partial S_a}{\partial x}$ rapidly changes in value, remaining again approximately constant across the capacity range of the voltage plateau. The cathode entropy remains close to zero within the capacity interval of the two main graphite phase transitions, which makes the anode the main contributor to the total cell entropy in this interval. Graphite dominated phase transitions in the anode manifest as changes S1-S3 on the entropy curve, although these features appear as even more pronounced transitions in the full-cell data than the anode half-cell data.

It is known that the phase transformations and lithium transport in graphite are slow, limited by grain boundaries in the material,[50] the staging dynamics of graphite[51,52] and exchange of ions at the

electrode/electrolyte interface.[53] In full-cell configurations, non-uniform lithium distributions in the anode material arise from different Ohmic drops and hence different local potentials at the centre versus the edges of the electrodes.[54] Consequently, inhomogeneous lithiation of graphite-based anodes has been reported, and because of slow relaxation processes, the resulting concentration gradients from even modest polarization can persist over hours or even days of relaxation time.[25,55,56] In commercial cells, these heterogeneities also persist over multiple length scales, as observable by X-ray tomography and neutron diffraction.[55,57] Making the anode area larger than the cathode, as is common in commercial cells, could lead to still greater inhomogeneous lithiation at the edges, as observed optically by Grimsmann et al..[58] The cell examined in the present study was found to have an anode area $\approx$790 cm^2 and cathode area $\approx$740 cm^2, resulting in an overhang $\approx$ 6%. The resulting non-uniform lithium distribution in the anode material could lead to higher lithium disorder and hence a greater entropy change due to disordered Stage II configurations;[25,59,60] anode overhang areas can also lead to reversible LLI.[61] The net result of all of these effects may lead to some disparities between combined entropy from half-cells and the full-cell entropy change, particularly at the boundaries between graphite phase transitions. Despite these differences, it is still possible to extract the information concerning which electrode drives the full-cell entropy because the phase boundaries on a voltage axis are clear from both the anode half-cell, and the full-cell data.

In terms of the transitions in the cathode material, the redox process during delithiation is mainly at the Ni (III)–Ni (IV) pair, accompanied by three distinct phase transformations.[62] First, there is a transition from hexagonal to monoclinic (H1 → M) starting at 0.4 Ah, then monoclinic to hexagonal (M → H2) at around 2.5 Ah, and lastly, hexagonal to hexagonal (H2 → H3) at 3.25 Ah.[63] The two last phase transitions do not appear to result in features in the full-cell entropy profile. However, the M → H2 transition is associated with a sharp transition in the partial molar enthalpy in the cathode material (Supplementary Material Fig. S1). This is advantageous because it allows changes in position and amplitude of transition S3 in the entropy profile (attributable to the main staging transition of graphite) to be probed in the absence of overlapping features from the cathode material.

Full-cell entropy results.—The reaction entropy measurements for the full-cell are plotted against voltage in Fig. 4. The voltage range shown is 3.4 V to 4.2 V since this is where features of interest

are present. Plotting entropy change against voltage allows for a more accurate comparison between charge and discharge by removing shifts in features with concentration.

Calendar ageing.—Figure 4a shows that the entropy measurements remain almost unchanged after calendar storage. A small increase in the entropy magnitude is observed ~3.87 V, denoted S3 in the preceding section, corresponding to the graphite stage I to stage II transition; however, this effect is nearly negligible. The most pronounced change in the data is a horizontal shift toward higher potentials and horizontal expansion on the voltage axis. Similarly to ICA, this observed horizontal shift and expansion indicates LLI.[64] There is a hysteresis in the entropy profile response, which is shown in the bottom panel of Fig. 4a. The resulting hysteresis is determined in Eq. 3 from the difference between the charge (ch) and discharge (dch) entropy change

$$\frac{\partial \Delta S_{hys}}{\partial x} = \frac{\partial \Delta S_{ch}}{\partial x} - \frac{\partial \Delta S_{dch}}{\partial x}. \qquad [3]$$

Since there are no significant changes to the entropy magnitude experienced by calendar aged cells, the entropy hysteresis also remains almost unchanged. These findings are consistent with the results presented by Sullivan et al.[20] studying a LCO cathode half-cell subjected to calendar ageing. The entropy profile shape and characteristic regions did not change when a substantial proportion of cell capacity was removed. It was concluded that the intercalation mechanisms in the aged cell remained the same.

Cycling ageing.—Figure 4b shows the effects of cycle ageing on entropy change. In contrast with the results shown for calendar ageing, the cycling ageing results indicate a more dramatic shift of all of the features toward higher potentials. Additionally, different changes in entropy magnitude are observed with respect to the direction of reaction. For full-cell discharge, we observe a gradual decrease and flattening of characteristic features. For charge, however, entropy change increases with cycling age with the most pronounced increase above 3.87 V.

Features near 3.87 V—The characteristic minimum in the entropy profile occurring ~3.87 V corresponds to the most pronounced graphite transition, stage I to stage II.[25,35,59] The cathode entropy change is featureless in this region. Therefore, the recorded entropy change variation most likely originates from microstructural changes to the graphite. With cycle age, the entropy minimum
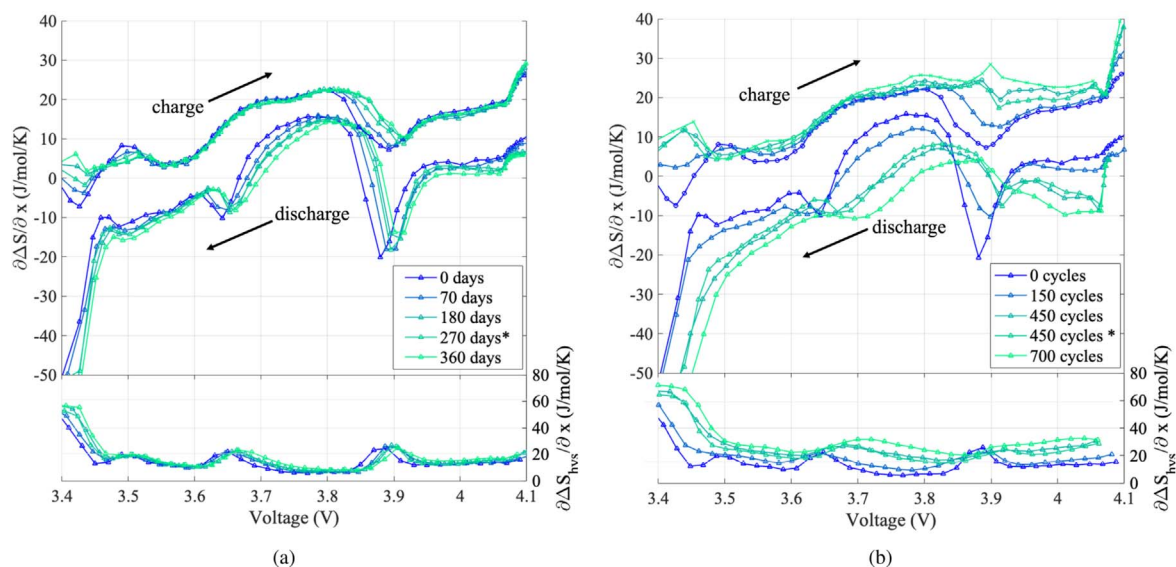
Figure 4. Charge and discharge entropy profile a) after several days of storage at 75 % SoC at 45 °C, b) after CCCV cycling at 45 °C. The bottom panel in a) and b) indicates entropy hysteresis, quantified by $\partial \Delta S_{hys}/\partial x$. * An unplanned 90 days of storage at 23 °C due to COVID-19.

increases (i.e. the step becomes less pronounced) and shifts positively in voltage.

Features below 3.87 V—To the left of the characteristic graphite stage I → stage II transition, there is a slight increase in the entropy change during charge (lithiation of the anode material). However, during discharge (anode delithiation), a more substantial decrease in entropy is seen as the cell ages.

Features above 3.87 V—At voltages above ~3.87 V, the full-cell entropy change continues to decrease with cycle age. For charge, an increase in entropy change is observed. For a pristine cell shown in Fig. 3, the entropy change contribution from the anode material is close to zero, and the full-cell entropy response is mainly due to the cathode material.

Impact of silicon on entropy profiles.—As a battery electrode material, graphite is an intercalating material, with Li inserting into its layered structure,[27] whereas silicon is an alloying material, experiencing solid-solution reactions with lithium.[27] The features of the OCP versus SoC, and the balance of lithium intercalated in Si and Gr at each SoC depend on the ratio of Gr to Si in the anode and also cycle direction.[29,65] Since Si is 10% wt of the anode but its gravimetric capacity is 10 times the graphite (372 mAh/g), the overall anode capacity is equally composed of 50% Si and 50% Gr.[66]

Anode delithiation Due to the similar contributions of Si and Gr to the anode capacity, delithiation happens sequentially,[15,27] that is to say, Gr dominates the initial stages of full-cell discharge in the range 4.2 V to 3.87 V (Fig. 4). Then, the capacity contribution from Si and Gr become comparable within 3.87 V to 3.65 V interval. Lastly, at < 3.65 V anode delithiation becomes completely dominated by Si.

Consequently, the discharge entropy change profile shown in Fig. 4b is a combination of both the Si and Gr reactions, where we observe steady entropy change flattening with cycling.

A possible explanation for this is mechanical changes in the anode particles, specifically breaking and cracking, as has been reported in other studies.[30,67] This is also often mentioned as a primary cause of Si particle inactivation in Gr-Si anodes.[15,68–70] Entropy profiling measures (among other contributions) the configurational degrees of freedom of lithium-vacancy arrangements in the electrode materials.[25,31,33,35,59] Microstructural changes reduce the number of accessible sites in the host material by causing point defects[34,44] and stacking faults (i.e. turbostratic disorder[71,72]). Given that there are only small entropy profile features from the cathode material at the start of life, we do not expect to detect changes to cathode morphology from entropy profiling, even if they are present. Changes to the surface structural ordering of graphite with repeated cycling have been reported elsewhere using Raman spectroscopy,[73,74] even when the C-rate is as low as C/37.[74] It is known that the Li-graphite stages are extremely sensitive to the stacking order of graphite.[71,72] The observed changes in entropy profiling with cycle ageing are consistent with the changes to the staging sequence that would be expected with this type of structural disordering, resulting in a reduced amplitude of the entropy change from those transitions. This trend is in accordance with the observed changes to the S3 feature at ~3.87 V.

Anode lithiation Because of the (de)lithiation hysteresis introduced by Si, the balance of lithium in Gr and Si at each full-cell voltage is very different during lithiation of the anode. Based on the stoichiometric model of lithium filling in Gr/Si blends presented by Jiang et al.,[27] lithiation proceeds simultaneously within Si and Gr in the interval 3.4 V to 4.1 V. However, over the same voltage interval, a greater fraction of Li is inserted into Si. According to the same model, it is only in the part of the anode half-cell voltage profile corresponding to full cell voltage (>4.1 V) that a greater fraction of lithium is into inserted into Gr. This explains the observed differences between charge and discharge entropy profiles. An increase in the entropy change with cycle ageing may suggest expansion of the Si particles with ageing, agreeing with Vorauer et

al.[40] The cited work suggests volume expansion is associated with a more inhomogenous distribution of lithium, and therefore, it is possible that this results in the observed increase in entropy change. Therefore, the discharge entropy measurements should be considered and analysed separately from the charge measurements.

Entropy hysteresis Over a broad voltage range, the entropy hysteresis increases with cycling. It is known that there is a negligible difference between graphite (de)lithiation entropy change above ~3.87 V in a full-cell,[25,35,59] but there is a hysteresis in pristine graphite at full-cell voltage ~3.87 V, which is attributed to metastable carbon stacking configurations.[25] We hypothesize that the main source of hysteresis visible in Fig. 4(b) originates from Si, given its large OCP hysteresis[70] over a broad voltage scale. However, during graphite transition II → I at ~3.87 V, and graphite transition III → II at ~3.65 V, the entropy hysteresis remains fairly constant with cycle age. This could be due to localised decrease in hysteresis from graphite in combination with increase in hysteresis from silicon across the entire voltage range. Since we cannot detect additional features in the anode half-cell entropy profiles compared with published data for pure Gr anodes, we attribute the observed behavior at 3.87 V and 3.65 V to the effect of microscopic Gr degradation.

Comparison of DVA and entropy profiling.—Entropy magnitudes and entropy hysteresis ageing data may be plotted against voltage, as above, giving insight into microstructural material changes. One can also compare data against capacity, giving insight into electrode stoichiometry changes (similar to DVA). Given that both DVA and entropy profiles are sensitive to phase transitions, a direct comparison between these two methods can be made using the Maxwell relation:

$$\frac{\partial^2 E_{\text{OCP}}}{\partial T \partial Q} = \frac{\partial^2 E_{\text{OCP}}}{\partial Q \partial T} \qquad [4]$$

The state of charge is expressed via Coulomb counting as $x = Q/Q_0$, where Q is the stored charge in the cell and Q_0 is the nominal capacity of the cell.

Substituting entropy change 1 and DVA Eqs. in 4 gives

$$\frac{\partial^2 E_{\text{OCP}}}{\partial T \partial Q} = \frac{\partial}{\partial T}\left(\frac{\partial E_{\text{OCP}}}{\partial Q}\right) = \frac{\partial}{\partial Q}\left(\frac{\partial E_{\text{OCP}}}{\partial T}\right)$$

$$\approx \frac{d}{dQ}\left(\frac{1}{nF}\frac{\partial(\Delta S)}{\partial x}\right) = \frac{1}{nF}\frac{d}{dQ}\left(\frac{\partial(\Delta S)}{\partial x}\right). \qquad [5]$$

To compare features in the entropy data with respect to the DVA, the right hand side of (5), i.e. $d(\partial \Delta S/\partial x)/dQ$, was computed and plotted with respect to capacity in Fig. 5. The phase transitions are identified through the DVA peaks. For consistency, entropy and DVA curves were all calculated from the same data extracted from GITT.

Since DVA is a well established diagnostic method, it is used here as a baseline for identification of degradation mechanisms experienced by aged cells. DVA curves for charge and discharge are shown in Fig. 5. In all test data, the cathode DVA peak D₄ shifts toward lower capacities with ageing. According to the literature,[17] a horizontal shift on a DVA curve is due to loss of cyclable lithium. The calendar aged cells exhibit less visible shifts, indicating less capacity loss than the cycled cells. A corresponding horizontal shift of marker dS₄ is observed in Fig. 5. The anode peak D₃, indicating the graphite stage II → I transition, decreases marginally in magnitude for the calendar aged group. This is followed by a proportionally smaller decrease of the dS₃ peak. In the cycled group, however, the DVA peak D₃ flattens to the point that it becomes difficult to distinguish. In the entropy plot, peak dS₃ is still well recognizable, although it decreases in magnitude from the pristine cell data. This suggests that the entropy change curve is more sensitive to anode phase transformations than the DVA curve.
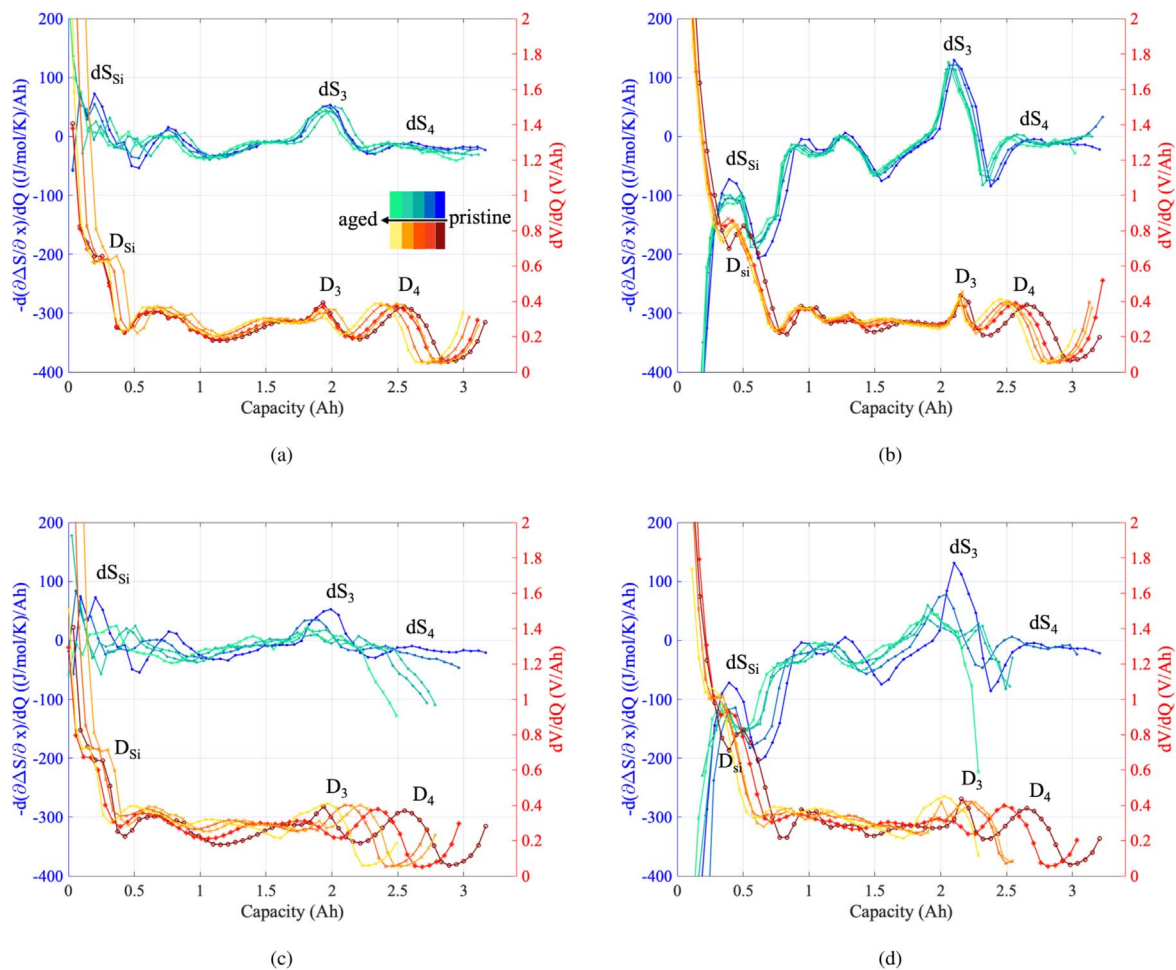
Figure 5. $d(\partial \Delta S/\partial x)/dQ$ and DVA plots for calendar aged cells a) charge b) discharge and cycle aged cells c) charge d) discharge.

The two DVA features D_3 and D_4 are crucial for the diagnosis of electrode specific degradation modes.[17,18] Loss of active material (LAM) in the positive electrode $Q_{LAM,PE}$ is calculated from the capacity difference between D_4 and Q_{full}, the maximum measured capacity. Similarly, at the negative electrode $Q_{LAM,NE}$ is identified as the change in capacity between D_3 and 0 Ah, while the shift between electrodes $Q_{balance}$ is the difference between the maximum capacity and $Q_{LAM,NE}$.

Following Keil et al.'s method,[17] the same procedure was applied to the entropy curves to extract ageing markers. From Fig. 5 it is clear that the anode peak D_3 corresponds to DVA peak dS_3 and so peak shifts indicate LAM_{NE}. The cathode peak D_4 occurs in the same region as the dS_4 peak, and is therefore used to calculate LAM_{PE}. The results obtained from both entropy and DVA markers are shown in Fig. 6. Despite some differences, the resemblance is noteworthy, confirming that entropy measurements can be successfully used for identification of degradation mechanisms.

Note that, due to the full-cell hysteresis emerging largely from Si in the anode material, the ageing markers may provide different information when calculated from charge vs. discharge data. However, the standard practice in the literature is to analyze only one direction of DVA profiles, most commonly charge.[12,16,30] Given that the main objective in this study is the comparison of extracted markers from both DVA and entropy profiling, we follow the same procedure, and use charge data only. However, we present extracted markers in terms of normalised capacity to account for differences between charge and discharge. Note that the Si marker in Fig. 5, dS_{Si}, occurs at low SoC and is strongly influenced by current direction. Shifts to this marker are difficult to quantify and interpret, and therefore are not considered in this study.

Analysis of ageing markers—Figure 6a shows the estimated ageing markers for the calendar aged cells. Capacity fade appears to be caused primarily by LLI, which manifests in electrode balancing changes. This confirms that the horizontal shift on the voltage axis observed in Fig. 4a is due to changes in electrode balancing. No further ageing markers are evident for the calendar aged cells, making LLI the main ageing mechanism. Figure 6b shows the ageing markers for the cycle-aged cells. Overall, there appears to be a decrease in LAM_{NE} with age, as has been found by others.[30,75] In our data, LAM_{PE} also decreases, indicating additional degradation of the cathode material. Lastly, a decrease in electrode balancing $Q_{LLIbalance}$ suggests lost Li inventory.

We note that there is an apparent "capacity recovery effect" between RPT3 and RPT4. This time period corresponds to an extended COVID-19 lab closure, during which two test conditions were changed simultaneously: the temperature was decreased from 45 °C to 23 °C and the SoC decreased from 75% to 50%. This resulted in calendar aged cells experiencing a recovery in LLI together with a less pronounced increase in LAM_{NE}. This suggests recovery of capacity from the "anode overhang" effect.[61] Geometrically, anode overhang is defined as an additional anode area which is not directly opposed by the cathode.[76] Given longer ionic pathways and therefore a very slow timescale for lateral diffusion from the anode overhang area to the useable battery area, under certain favourable conditions, some capacity can be regained.[76] This effect is also present in the cycled cells between RPT3 and RPT4; however, LAM_{NE} remains constant in that case.

SEM analysis.—To validate the degradation signatures obtained from entropy profiling, a post-mortem analysis was conducted on
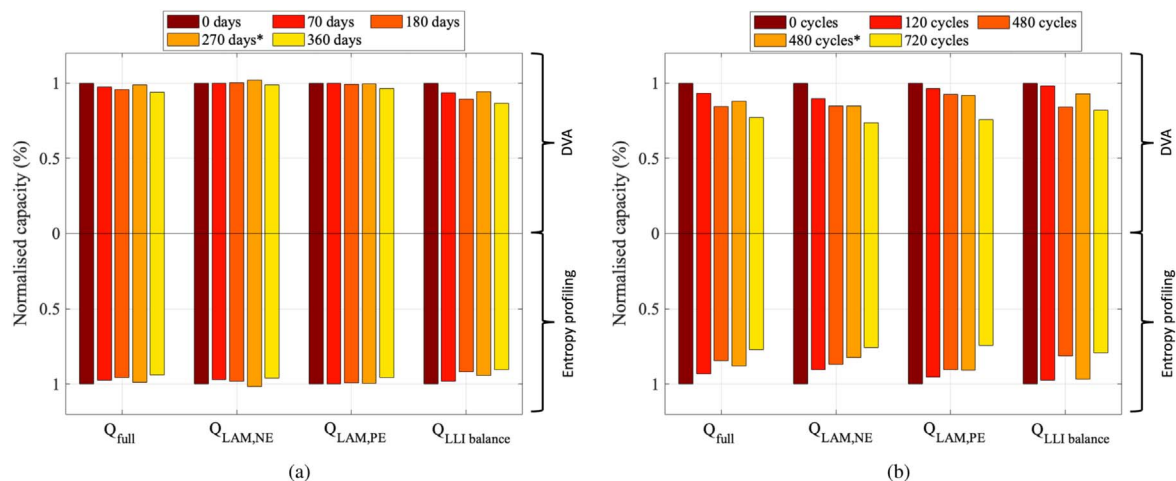
Figure 6. A comparison of ageing markers extracted from DVA and entropy profiling for calendar aged (a) and cycle aged (b) groups of cells. In both cases, the charge profiles were used to extract the ageing markers.

one cell from each of the interest groups, i.e. pristine, calendar aged and cycle aged. The morphologies of both the negative and positive electrodes were studied using SEM. Figure 7a shows the surface of the pristine anode material. In this image, the Gr edges are sharp and well defined. The image of the calendar aged material is presented in Fig. 7b, which shows that the sharp edges of Gr become less prominent. The coarse particles can be ascribed to the formation of the SEI layer. Consequently, the surface film thickness increases from 82 μm to 86 μm. These observations correspond well with the dominant degradation mode identified by DVA and entropy profiling, namely LLI. Finally, Fig. 7c shows the impact of cycle ageing, where surface film formation becomes significant, also consistent with LLI. Consequently, the coating thickness increased to 90 μm, i.e. slightly thicker than the calendar aged film. Given that the LLI in the calendar and cycle aged materials was similar, we

attribute the difference between the two instead to greater volume expansion from cycle ageing.

The size range of the SiO_x particles is between 1–9 μm, which makes it difficult to assess pulverisation from Figs. 7a–7c. Figures 7d–7f show the back scattered electron (BSE-SEM) images of the pristine, calendar and cycle aged electrodes, respectively. In the pristine sample, the SiO_x particles are visibly brighter than the surrounding graphite particles because of the higher atomic number of Si compared with carbon, and hence greater electron back scattering.

The SiO_x particles in the pristine sample are brighter compared with the calendar aged and cycle aged ones. The difference in brightness can be attributed to the pulverisation of the densely packed SiO_x aggregates upon electrochemical cycling, which leads to disconnection of particles via vacancies left behind by lithium-ion
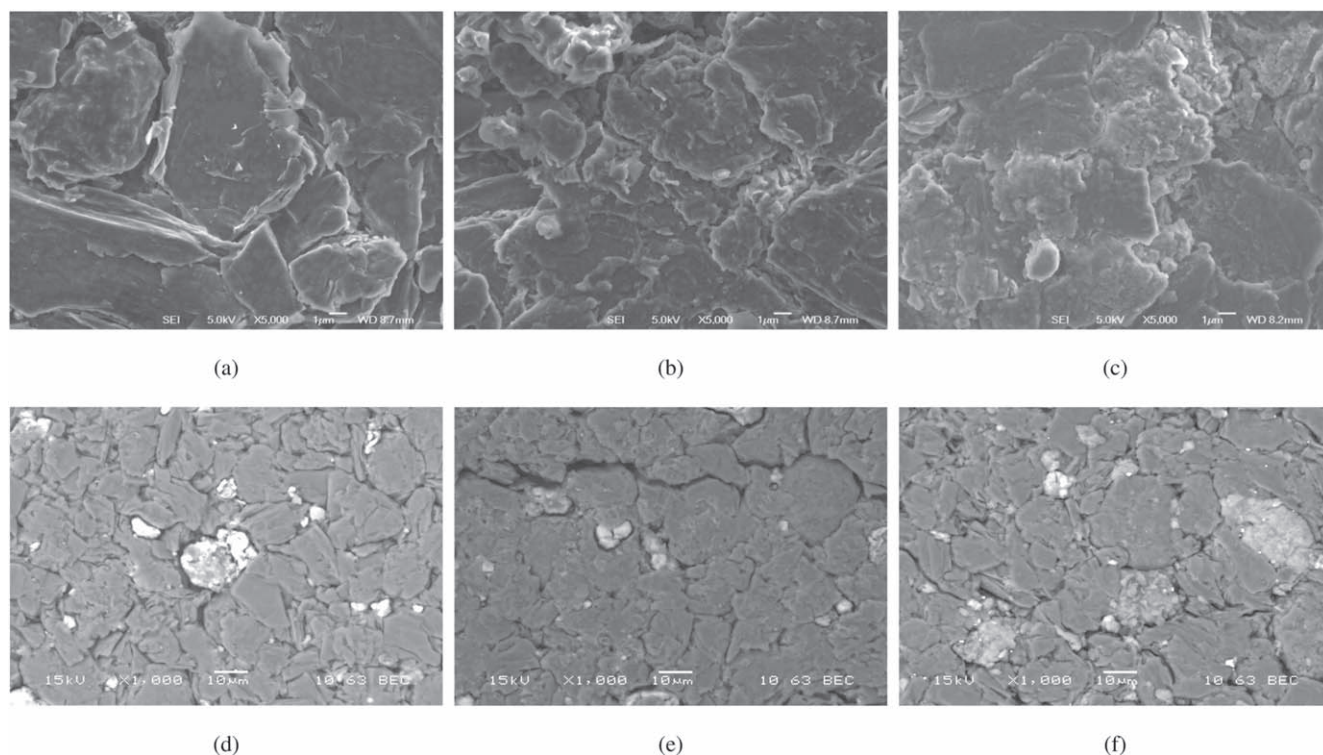
Figure 7. SEM images for Gr/Si anode a) pristine b) calendar aged c) cycle aged and BSE-SEM images for Gr/Si anode d) pristine e) calendar aged f) cycle aged.

stripping.[77] This lithiation driven fracture in SiO_x particles results in a newly exposed active material surface, which leads to further SEI formation. The SEI is composed of lighter elements compared to Si and therefore SEI growth results in a darker image compared to the brighter pristine electrode. It has been reported in the literature that a large part of the film growth on Si/C anodes is due to the formation of lithium silicates,[78,79] which could also account for the LAM observed in the entropy/DVA analysis.

In contrast to the anode, no thickness changes were observed on the cathodes across pristine versus aged cells.

Conclusions

In this study of silicon-graphite/NCA Li-ion batteries and half-cells constructed from harvested electrode materials, we measured the open circuit voltage and entropy changes that occur during calendar and cyclic ageing. Comparison of half- and full-cell entropy data reveals that the entropy measurements associated with the NCA cathode are almost uniform as a function of capacity, in contrast to anode entropy measurements. Thus the full-cell entropy measurements are dominated by anode-related features during both charge and discharge.

We found a significant difference between the measured entropy profiles during charge versus discharge, indicating an "entropy hysteresis" related to path-dependent reaction mechanisms in the electrode materials. Changes to the entropy hysteresis with age were used to infer qualitative changes to the cell material morphology.

For the calendar-aged cells, the entropy profile magnitudes remained almost unchanged with age, but slight shifts versus voltage were found. Additionally, the entropy hysteresis remained unchanged with age. These results imply that the microstructure of the electrode materials did not change substantially with age.

In contrast, in cycle-ageing data, our investigation revealed a decrease in entropy magnitude during discharge and increase during charge, with greater shifts in observable features as a function of voltage than were found during calendar ageing. The combination of the shift and amplitude change may be attributed to particle breaking and cracking induced by cycling, with concomitant microstructural changes to the anode material. We hypothesize that the changes to graphite-related entropy features originate from microstructural defects. The overall increase in entropy hysteresis may be related to Si volume expansion effects, however further research is required to establish the exact dependency of entropy features on particle size and Si mass fraction.

A direct comparison between entropy profiling and DVA reveals that in general, both techniques highlight similar features of battery behavior. Entropy profiling can thus successfully track ageing markers such as LAM_{PE}, LAM_{NE} and LLI. Using these techniques, both DVA and entropy profiling highlighted LLI as the main degradation mode for calendar aged cells. Cycled cells on the other hand experienced LAM_{NE} and LAM_{PE} combined with LLI. Notably, the entropy magnitude was found to provide greater sensitivity to changes and features at some operating voltages, and these features are not accessible by DVA.

However, entropy changes are time-consuming to measure and require specialist equipment. To be competitive with DVA, the measurement time needs to be further decreased. A possible future avenue to be explored is systematic studies of graphite/silicon half-cells using entropy profiling (and comparison with full-cell behavior) in order to decouple silicon and graphite contributions.

Acknowledgments

ORCID

Malgorzata E. Wojtala ⓘ https://orcid.org/0000-0001-8371-206X
Alana A. Zülke ⓘ https://orcid.org/0000-0003-2274-0002
Robert Burrell ⓘ https://orcid.org/0000-0001-9004-3466
Guanchen Li ⓘ https://orcid.org/0000-0001-8125-6793
Harry E. Hoster ⓘ https://orcid.org/0000-0001-6379-5275
David A. Howey ⓘ https://orcid.org/0000-0002-0620-3955
Michael P. Mercer ⓘ https://orcid.org/0000-0001-7578-3554

References

1. H. A. Gabbar, A. M. Othman, and M. R. Abdussami, "Review of Battery Management Systems (BMS) Development and Industrial Standards." *Technologies*, **9**, 28 (2021).
2. F. Baronti, C. Bernardeschi, L. Cassano, A. Domenici, R. Roncella, and R. Saletti, "Design and safety verification of a distributed charge equalizer for modular li-ion batteries." *IEEE Trans. Industr. Inform.*, **10**, 1003 (2014).
3. A. Barré, B. Deguilhem, S. Grolleau, M. Gérard, F. Suard, and D. Riu, "A review on lithium-ion battery ageing mechanisms and estimations for automotive applications." *J. Power Sources*, **241**, 680 (2013).
4. M. Lucu, E. Martinez-Laserna, I. Gandiaga, and H. Camblong, "A critical review on self-adaptive Li-ion battery ageing models." *J. Power Sources*, **401**, 85 (2018).
5. M. Muratori et al., "The rise of electric vehicles2020 status and future expectations.." *Prog. Energy*, **3**, 022002 (2021).
6. M. Ebner, F. Marone, M. Stampanoni, and V. Wood, "Visualization and quantification of Electrochemical and Mechanical." *Science*, **342**, 716 (2013).
7. S. Zhang, K. Zhao, T. Zhu, and J. Li, "Electrochemomechanical degradation of high-capacity battery electrode materials." *Prog. Mater. Sci.*, **89**, 479 (2017).
8. F. Lin, K. Zhao, and Y. Liu, "Heterogeneous reaction activities and statistical characteristics of particle cracking in battery electrodes." *ACS Energy Lett.*, **6**, 4065 (2021).
9. M. Ecker, N. Nieto, S. Käbitz, J. Schmalstieg, H. Blanke, A. Warnecke, and D. U. Sauer, "Calendar and cycle life study of Li(NiMnCo)O2-based 18 650 lithium-ion batteries." *J. Power Sources*, **248**, 839 (2014).
10. P. M. Attia, B. Alexander, F. Brosa-Planella, G. Dechent, M. Dos Reis, M. Dubarry, P. Gasper, R. Gilchrist, S. Greenbank, and D. Howey, "Review—"Knees" in Lithium-Ion Battery Aging Trajectories." *J. Electrochem. Soc.*, **169**, 60517 (2022).
11. M. Dubarry and D. Beck, "Analysis of synthetic voltage vs. capacity datasets for big data li-ion diagnosis and prognosis." *Energies*, **14**, 2371 (2021).
12. I. Bloom, A. N. Jansen, D. P. Abraham, J. Knuth, S. A. Jones, V. S. Battaglia, and G. L. Henriksen, "Differential voltage analyses of high-power, lithium-ion cells 1. Technique and application." *J. Power Sources*, **139**, 295 (2005).
13. I. Bloom, J. Christophersen, and K. Gering, "Differential voltage analyses of high-power lithium-ion cells 2. Applications." *J. Power Sources*, **139**, 304 (2005).
14. M. Dubarry, C. Truchot, and B. Y. Liaw, "Synthesize battery degradation modes via a diagnostic and prognostic model." *J. Power Sources*, **219**, 204 (2012).
15. J. Schmitt, M. Schindler, and A. Jossen, "Change in the half-cell open-circuit potential curves of silicon-graphite and nickel-rich lithium nickel manganese cobalt oxide during cycle aging." *J. Power Sources*, **506**, 230240 (2021).
16. P. Keil, S. F. Schuster, J. Wilhelm, J. Travi, A. Hauser, R. C. Karl, and A. Jossen, "Calendar aging of lithium-ion batteries." *J. Electrochem. Soc.*, **163**, A1872 (2016).
17. P. Keil and A. Jossen, "Calendar aging of nca lithium-ion batteries investigated by differential voltage analysis and coulomb tracking." *J. Electrochem. Soc.*, **164**, A6066 (2017).
18. A. Zülke, Y. Li, P. Keil, R. Burrell, S. Belaisch, M. Nagarathinam, M. P. Mercer, and H. E. Hoster, "High-energy nickel-cobalt-aluminium oxide (NCA) cells on idle: anode- versus cathode-driven side reactions." *Batter. Supercaps*, **4**, 934 (2021).
19. B. Wu, Y. Yufit, Y. Merla, R. F. Martinez-Botas, N. P. Brandon, and G. J. Offer, "Differential thermal voltammetry for tracking of degradation in lithium-ion batteries." *J. Power Sources*, **273**, 495 (2015).
20. J. P. Sullivan et al., "The science of battery degradation." *Technical Report January* (Sandia National Laboratories, Livermore) (2015).
21. K. Maher and R. Yazami, "A study of lithium ion batteries cycle aging by thermodynamics techniques." *J. Power Sources*, **247**, 527 (2014).
22. X. F. Zhang, Y. Zhao, Y. Patel, T. Zhang, W. M. Liu, M. Chen, G. J. Offer, and Y. Yan, "Potentiometric measurement of entropy change for lithium batteries." *Phys. Chem. Chem. Phys.*, **19**, 9833 (2017).
23. P. J. Osswald, M. Del Rosario, J. Garche, A. Jossen, and H. E. Hoster, "Fast and accurate measurement of entropy profiles of commercial lithium-ion cells." *Electrochim. Acta*, **177**, 270 (2015).
24. G. Assat, S. L. Glazier, C. Delacourt, and J. M. Tarascon, "Probing the thermal effects of voltage hysteresis in anionic redox-based lithium-rich cathodes using isothermal calorimetry.." *Nat. Energy*, **4**, 647 (2019).
25. M. P. Mercer, C. Peng, C. Soares, H. E. Hoster, and D. Kramer, "Voltage hysteresis during lithiation/delithiation of graphite associated with meta-stable carbon stackings." *J. Mater. Chem. A*, **9**, 492 (2021).
26. Y. Jiang, G. Offer, J. Jiang, M. Marinescu, and H. Wang, "Voltage hysteresis model for silicon electrodes for lithium ion batteries, including multi-step phase transformations, crystallization and amorphization." *J. Electrochem. Soc.*, **167**, 130533 (2020).
27. J. Yang, Z. Niu, G. Offer, J. Xuan, and H. Wang, "Insights into the role of silicon and graphite in the electrochemical performance of silicon/graphite blended

electrodes with a multi-material porous electrode model." *J. Electrochem. Soc.*, **169**, 020568 (2022).

28. D. Allart, M. Montaru, and H. Gualous, "Model of lithium intercalation into graphite by potentiometric analysis with equilibrium and entropy change curves of graphite electrode." *J. Electrochem. Soc.*, **165**, A380 (2018).

29. E. Moyassari, T. Roth, S. Kücher, C. Chang, S. Hou, F. B. Spingler, and A. Jossen, "The role of silicon in silicon-graphite composite electrodes regarding specific capacity, cycle stability, and expansion." *J. Electrochem. Soc.*, **169**, 010504 (2022).

30. T. Raj, A. A. Wang, C. W. Monroe, and D. A. Howey, "Investigation of path-dependent degradation in lithium-ion batteries." *Batter. Supercaps*, **3**, 1377 (2020).

31. K. E. Thomas and J. Newman, "Heats of mixing and of entropy in porous insertion electrodes." *J. Power Sources*, **119-121**, 849 (2003).

32. S. Goutam, N. Omar, P. Van Den Bossche, and J. Van Mierlo, "Chapter two—review of nanotechnology for anode materials in batteries." *Emerging Nanotechnologies in Rechargeable Energy Storage Systems, Micro and Nano Technologies*, ed. L. M. Rodriguez-Martinez and N. Omar (Elsevier, Boston) p 45 (2017).

33. Y. Reynier, J. Graetz, S. Tabitha, P. Rez, R. Yazami, and B. Fultz, "Entropy of Li intercalation in LixCoO2." *Phys. Rev. B*, **70**, 174304 (2004).

34. M. P. Mercer, S. Finnigan, D. Kramer, D. Richards, and H. E. Hoster, "The influence of point defects on the entropy profiles of Lithium Ion Battery cathodes: a lattice-gas Monte Carlo study." *Electrochim. Acta*, **241**, 141 (2017).

35. M. P. Mercer, M. Otero, M. Ferrer-Huerta, A. Sigal, D. E. Barraco, H. E. Hoster, and E. P. M. Leiva, "Transitions of lithium occupation in graphite: A physically informed model in the dilute lithium occupation limit supported by electrochemical and thermodynamic measurements." *Electrochim. Acta*, **324**, 134774 (2019).

36. B. Orvananos, H. C. Yu, R. Malik, A. Abdellahi, C. P. Grey, G. Ceder, and K. Thornton, "Effect of a size-dependent equilibrium potential on nano-LiFePO4 particle interactions." *J. Electrochem. Soc.*, **162**, A1718 (2015).

37. F. Grimsmann, F. Brauchle, T. Gerbert, A. Gruhle, M. Knipper, and J. Parisi, "Hysteresis and current dependence of the thickness change of lithium-ion cells with graphite anode." *J. Energy Storage*, **12**, 132 (2017).

38. S. Schweidler, L. de Biasi, A. Schiele, P. Hartmann, T. Brezesinski, and J. Janek, "Volume changes of graphite anodes revisited: a combined operando x-ray diffraction and in situ pressure analysis study." *J. Phys. Chem. C*, **122**, 8829 (2018).

39. D. Y. W. Yu, M. Zhao, and H. E. Hoster, "Suppressing vertical displacement of lithiated silicon particles in high volumetric capacity battery electrodes." *ChemElectroChem*, **8**, 1090 (2015).

40. T. Vorauer et al., "Multi-scale quantification and modeling of aged nanostructured silicon-based composite anodes." *Commun. Chem.*, **3**, 1 (2020).

41. G. M. Veith, M. Doucet, R. L. Sacci, B. Vacaliuc, J. K. Baldwin, and J. F. Browning, "Determination of the solid electrolyte interphase structure grown on a silicon electrode using a fluoroethylene carbonate additive." *Sci. Rep.*, **7**, 1 (2017).

42. K. Kalaga, M. F. Rodrigues, S. E. Trask, I. A. Shkrob, and D. P. Abraham, "Calendar-life versus cycle-life aging of lithium-ion cells with silicon-graphite composite electrodes." *Electrochim. Acta*, **280**, 221 (2018).

43. A. Zülke, Y. Li, P. Keil, and H. Hoster, "Communication—why high-precision coulometry and lithium plating studies on commercial lithium-ion cells require thermal baths." *J. Electrochem. Soc.*, **166**, A2921 (2019).

44. S. Schlueter, R. Genieser, D. Richards, H. E. Hoster, and M. P. Mercer, "Quantifying structure dependent responses in Li-ion cells with excess Li spinel cathodes: matching voltage and entropy profiles through mean field models." *Phys. Chem. Chem. Phys.*, **20**, 21417 (2018).

45. M. P. Mercer, S. Affleck, E. M. Gavilán-Arriazu, A. A. Zülke, P. A. Maughan, S. Trivedi, M. Fichtner, A. R. Munnangi, E. P. M. Leiva, and H. E. Hoster, "Sodiation of hard carbon: How separating enthalpy and entropy contributions can find transitions hidden in the voltage profile." *ChemPhysChem*, **23**, e202100748 (2022).

46. C. Didier, W. K. Pang, Z. Guo, S. Schmid, and V. K. Peterson, "Phase evolution and intermittent disorder in electrochemically lithiated graphite determined using in operando neutron diffraction." *Chem. Mater.*, **32**, 2518 (2020).

47. K. G. Gallagher, D. W. Dees, A. N. Jansen, D. P. Abraham, and S. Kang, "A volume averaged approach to the numerical modeling of phase-transition intercalation electrodes presented for LixC6." *J. Electrochem. Soc.*, **159**, A2029 (2012).

48. J. Lim et al., "Origin and hysteresis of lithium compositional spatiodynamics within battery primary particles." *Science*, **353**, 566 (2016).

49. J. R. Dahn, "Phase diagram of LixC6." *Phys. Rev. B*, **44**, 9170 (1991).

50. K. Persson, V. A. Sethuraman, L. J. Hardwick, Y. Hinuma, A. Meng, Y. S. van der Ven, V. Srinivasan, R. Kostecki, and G. Ceder, "Lithium diffusion in graphitic carbon." *J. Phys. Chem. Lett.*, **1**, 1176 (2010).

51. E. M. Gavilan-Arriazu, M. P. Mercer, O. A. Pinto, O. A. Oviedo, D. E. Barraco, H. E. Hoster, and E. P. M. Leiva, "Effect of temperature on the kinetics of electrochemical insertion of li-ions into a graphite electrode studied by kinetic monte carlo." *J. Electrochem. Soc.*, **167**, 013533 (2019).

52. G. Yinsheng, R. B. Smith, Z. Yu, D. K. Efetov, J. Wang, P. Kim, M. Z. Bazant, and L. E. Brus, "Li intercalation into graphite: Direct optical imaging and cahn-hilliard reaction dynamics." *J. Phys. Chem. Lett.*, **7**, 2151 (2016).

53. E. M. Gavilan-Arriazu, O. A. Pinto, B. A. López de Mishima, D. E. Barraco, O. A. Oviedo, and E. P. M. Leiva, "The kinetic origin of the daumas-hérold model for the li-ion/graphite intercalation system." *Electrochem. Commun.*, **93**, 133 (2018).

54. P. J. Osswald, S. V. Erhard, J. Wilhelm, H. E. Hoster, and A. Jossen, "Simulation and measurement of local potentials of modified commercial cylindrical cells." *J. Electrochem. Soc.*, **162**, A2099 (2015).

55. J. Wilhelm, S. Seidlmayer, S. Erhard, M. Hofmann, R. Gilles, and A. Jossen, "In situ neutron diffraction study of lithiation gradients in graphite anodes during discharge and relaxation." *J. Electrochem. Soc.*, **165**, A1846 (2018).

56. P. J. Osswald, S. V. Erhard, A. Rheinfeld, B. Rieger, H. E. Hoster, and A. Jossen, "Temperature dependency of state of charge inhomogeneities and their equalization in cylindrical lithium-ion cells." *J. Power Sources*, **329**, 546 (2016).

57. S. Müller, J. Eller, M. Ebner, C. Burns, J. Dahn, and V. Wood, "Quantifying inhomogeneity of lithium ion battery electrodes and its influence on electrochemical performance." *J. Electrochem. Soc.*, **165**, A339 (2018).

58. F. Grimsmann, T. Gerbert, F. Brauchle, A. Gruhle, J. Parisi, and M. Knipper, "Hysteresis and current dependence of the graphite anode color in a lithium-ion cell and analysis of lithium plating at the cell edge." *J. Energy Storage*, **15**, 17 (2018).

59. R. Yazami and Y. Reynier, "Thermodynamics and crystal structure anomalies in lithium-intercalated graphite." *J. Power Sources*, **153**, 312 (2006).

60. Y. Reynier, R. Yazami, and B. Fultz, "XRD evidence of macroscopic composition inhomogeneities in the graphite-lithium electrode." *J. Power Sources*, **165**, 616 (2007), IBA—HBC 2006.

61. R. Burrell, A. Zulke, P. Keil, and H. Hoster, "Communication identifying and managing reversible capacity losses that falsify cycle ageing tests of lithium-ion cells." *J. Electrochem. Soc.*, **167**, 130544 (2020).

62. A. Grenier, H. Liu, K. M. Wiaderek, Z. W. Lebens-Higgins, O. J. Borkiewicz, L. F. Piper, P. J. Chupas, and K. W. Chapman, "Reaction heterogeneity in LiNi0.8Co0.15Al0.05O2 induced by surface layer." *Chem. Mater.*, **29**, 7345 (2017).

63. P. Xiao, T. Lv, X. Chen, and C. Chang, "LiNi0.8Co0.15Al0.05O2: enhanced electrochemical performance from reduced cationic disordering in Li Slab." *Sci. Rep.*, **7**, 1 (2017).

64. A. J. Smith, P. Svens, M. Varini, G. Lindbergh, and R. W. Lindström, "Expanded In situ aging indicators for lithium-ion batteries with a blended NMC-LMO electrode cycled at sub-ambient temperature." *J. Electrochem. Soc.*, **168**, 110530 (2021).

65. J. Moon et al., "Interplay between electrochemical reactions and mechanical responses in silicon-graphite anodes and its impact on degradation." *Nat. Commun.*, **12**, 2714 (2021).

66. X. Zhang, D. Wang, X. Qiu, Y. Ma, D. Kong, K. Müllen, X. Li, and L. Zhi, "Stable high-capacity and high-rate silicon-based lithium battery anodes upon two-dimensional covalent encapsulation." *Nat. Commun.*, **11**, 1 (2020).

67. X. Li, A. M. Colclasure, D. P. Finegan, D. Ren, Y. Shi, X. Feng, L. Cao, Y. Yang, and K. Smith, "Degradation mechanisms of high capacity 18 650 cells containing Si-graphite anode and nickel-rich NMC cathode." *Electrochim. Acta*, **297**, 1109 (2019).

68. J. D. McBrayer et al., "Calendar aging of silicon-containing batteries." *Nat. Energy*, **6**, 866 (2021).

69. M. N. Obrovac and V. L. Chevrier, "Alloy negative electrodes for Li-ion batteries." *Chem. Rev.*, **114**, 11444 (2014).

70. M. T. F. Rodrigues, J. A. Gilbert, K. Kalaga, and D. P. Abraham, "Insights on the cycling behavior of a highly-prelithiated silicon-graphite electrode in lithium-ion cells." *J. Phys. Energy*, **2**, 024002 (2020).

71. T. Zheng, J. N. Reimers, and J. R. Dahn, "Effect of turbostratic disorder in graphitic carbon hosts on the intercalation of lithium." *Phys. Rev. B*, **51**, 734 (1995).

72. T. Zheng and J. R. Dahn, "Effect of turbostratic disorder on the staging phase diagram of lithium-intercalated graphitic carbon hosts." *Phys. Rev. B*, **53**, 3061 (1996).

73. V. A. Sethuraman, L. J. Hardwick, V. Srinivasan, and R. Kostecki, "Surface structural disordering in graphite upon lithium intercalation/deintercalation." *J. Power Sources*, **195**, 3655 (2010).

74. L. J. Hardwick, H. Buqa, and P. Novák, "Graphite surface disorder detection using in situ raman microscopy." *Solid State Ion.*, **177**, 2801 (2006).

75. E. Sarasketa-Zabala, F. Aguesse, I. Villarreal, R. Martinez, C. M. López, and C. P. Kubiak, "Understanding lithium inventory loss and sudden performance fade in cylindrical cells during cycling with deep-discharge steps." *J. Phys. Chem. C*, **119**, 896 (2015).

76. M. Lewerenz, G. Fuchs, L. Becker, and D. U. Sauer, "Irreversible calendar aging and quantification of the reversible capacity loss caused by anode overhang." *J. Energy Storage*, **18**, 149 (2018).

77. C. Y. Chen et al., "In situ scanning electron microscopy of silicon anode reactions in lithium-ion batteries during charge/discharge processes." *Sci. Rep.*, **6**, 1 (2016).

78. K. Richter, T. Waldmann, N. Paul, N. Jobst, R. G. Scurtu, M. Hofmann, R. Gilles, and M. Wohlfahrt-Mehrens, "Low-temperature charging and aging mechanisms of Si/C composite anodes in Li-Ion batteries: an operando neutron scattering study." *ChemSusChem*, **13**, 529 (2020).

79. K. Richter, T. Waldmann, M. Kasper, C. Pfeifer, M. Memm, P. Axmann, and M. Wohlfahrt-Mehrens, "Surface film formation and dissolution in Si/C anodes of Li-Ion batteries: a glow discharge optical emission spectroscopy depth profiling study." *J. Phys. Chem C*, **123**, 18795 (2019).